Atmos. Meas. Tech. Discuss., 8, 11323–11368, 2015
www.atmos-meas-tech-discuss.net/8/11323/2015/
doi:10.5194/amtd-8-11323-2015

Atmospheric Measurement Techniques Discussions

Comparison of Vaisala radiosondes RS41 and RS92 at the ARM Southern Great Plains Site

M. P. Jensen[1], D. Holdridge[2], P. Survo[3], R. Lehtinen[3], S. Baxter[1,4], T. Toto[1], and K. L. Johnson[1]

[1]Brookhaven National Laboratory, Upton, NY, USA
[2]Argonne National Laboratory, Argonne, IL, USA
[3]Vaisala Oyj, Helsinki, Finland
[4]State University of New York, Geneseo, NY, USA

Received: 31 August 2015 – Accepted: 2 October 2015 – Published: 2 November 2015

Correspondence to: M. P. Jensen (mjensen@bnl.gov)

Published by Copernicus Publications on behalf of the European Geosciences Union.

Abstract

In the fall of 2013, the Vaisala RS41-SG (4th generation) radiosonde was introduced as a replacement for the RS92-SGP radiosonde with improvements in measurement accuracy of profiles of atmospheric temperature, humidity and pressure. In order to help characterize these improvements, an intercomparison campaign was undertaken at the US Department of Energy's Atmospheric Radiation Measurement (ARM) Facility site in north Central Oklahoma USA. During 3–8 June 2014, a total of 20 twin-radiosonde flights were performed in a variety of atmospheric conditions representing typical mid-latitude continental summertime conditions. The results suggest that the RS92 and RS41 measurements generally agree within manufacturer specified tolerances with notable exceptions when exiting liquid cloud layers where the "wet bulbing" effect is mitigated in the RS41 observations. The RS41 measurements also appear to show a smaller impact from solar heating. These results suggest that the RS41 does provide important improvements, particularly in cloudy conditions, but under most observational conditions the RS41 and RS92 measurements agree within the manufacturer specified limits and so a switch to RS41 radiosondes will have little impact on long-term observational records.

1 Introduction

Since the 1930s measurements of tropospheric temperature, pressure, water vapor and winds have been made by radiosondes attached to balloons. These measurements provide critical input to weather forecasting and climate models, quantification of atmospheric thermodynamic stability, input to remote sensing retrievals and important constraints for atmospheric process studies. The long history of radiosonde observations includes many changes in instrumentation, practices, processing and other issues (e.g., Elliot and Gaffen, 1991, 1993; Elliot et al., 1998; Wang et al., 2003; Rowe et al., 2008; McCarthy et al., 2009; Milosevich et al., 2009; Zhao et al., 2012).

The US Department of Energy's Atmospheric Radiation Measurement (ARM) Climate Research Facility (Mather and Voyles, 2013; Ackerman and Stokes, 2003; Stokes and Schwartz, 1994; http://www.arm.gov) operates three fixed field sites (Southern Great Plains (SGP) Oklahoma, USA; North Slope, Alaska, USA; and Eastern North Atlantic, Azores, Portugal) and three mobile field sites to study the effects of aerosols, precipitation, surface fluxes and clouds on global climate. One important component of the measurements at each of these sites is the routine launching of radiosondes 2–4 times per day resulting in more than 5000 launches per year. During this period the ARM program has used Vaisala radiosondes as part of regular operations and intensive operational periods (e.g., Ghan et al., 2000; Xu et al., 2002; Xie et al., 2005; Miller et al., 2007; Jensen et al., 2015a, b). The RS92-SGP radiosonde is the current standard at all of the ARM sites and has been in use since 2005. The observations from these soundings have been used for many scientific applications including the derivation of large-scale forcing datasets for modeling studies (e.g., Zhang and Lin, 1997; Zhang et al., 2001; Xie et al., 2010, 2015), constraints on cloud remote sensing retrievals (e.g., Zhao et al., 2012; Huang et al., 2012; Dunn et al., 2011) and quantification of atmospheric thermodynamic structure (e.g., Sawyer and Li, 2013; McFarlane et al., 2013).

The Vaisala RS41-SG (4th generation) radiosonde was first developed to replace the RS92-SGP and was introduced in the fall of 2013 with new technological solution aimed at delivering improvements in measurement accuracy of profiles of atmospheric temperature, humidity and pressure. In order to characterize the improvements and differences of the RS41-SG radosonde compared to the RS92-SGP, a number of intercomparison campaigns have been undertaken in varying environments, including midlatitude test campaigns at Libus, Prague Czech Republic (Motl, 2014), in August 2013 and by the UK Met Office at Camborne, UK (Edwards et al., 2014) in November 2013. Higher latitude testing has been done in Finland (Vantaa and Sodankyla) and tropical conditions were sampled in Penang, Malaysia (Jauhiainen et al., 2014). This manuscript will describe the results of an intercomparison study of the new RS41-SG

(hereafter RS41) and RS92-SGP (hereafter RS92) Vaisala radiosondes at north Central Oklahoma, USA in June 2014 (Jensen, 2015). This new study distinguishes itself through a focus on a midlatitude summertime convective environment and the ability to leverage independent observations of clouds and atmospheric state from the ARM Climate Research Facility. Section 2 describes the differences between the two radiosonde types. Section 3 describes the experimental design and Sect. 4 describes the results of the intercomparison. Section 5 summarizes and discusses the implications of the results.

2 Differences between the RS92 and RS41 radiosondes

Figure 1 shows a picture of the two radiosonde types. The RS41/MW41 radiosondes/systems include improved sensor technologies and operational sounding preparations, compared to the RS92/MW31, aimed at improved accuracy and data consistency, and ease of operator preparation. Table 1 summarizes some of the key physical characteristics of the two radiosonde models. The RS41 is lighter and thinner than the RS92 and includes a smaller internal lithium battery compared to a separate alkaline battery for the RS92, which must be attached during launch preparation. The sensor characteristics for the two radiosondes are compared in Tables 2–4. The RS41 uses a resistive platinum temperature sensor compared to a capacitive wire sensor for the RS92. The RS41 temperature sensor has improved resolution and accuracy, but slightly slower response time compared to the RS92 (Table 2, Vaisala, 2014). For humidity observations the RS41 uses a thin-film capacitor with an integrated T sensor and heating functionality while the RS92 uses a thin-film capacitor with a heated twin sensor. The sensor heating capability of the RS41 is used for deicing when a radiosonde traverses through cloud layers with freezing conditions. The RS41 sensor has improved resolution, improved response time and accuracy compared with the RS92 (Table 3, Vaisala, 2014). The RS41 uses GPS observation of vertical displacement along with the temperature and humidity measurements to derive the atmospheric pressure (note

that there is also a model RS41-SGP radiosonde with a pressure sensor similar to the RS92) while the RS92 uses a silicon, capacitive sensor. The GPS-derived values of the RS41 have improved resolution and improved accuracy at pressures lower than 100 mb compared to the RS92 sensor measured pressure (Table 4, Vaisala, 2014). Both the RS41 and RS92 use GPS to derive wind speed and direction with similar measurement performance (velocity uncertainty = 0.15 m s^{-1}, direction uncertainty = 2 deg, Vaisala, 2014).

In general, the two radiosonde models apply similar types of corrections for the edited pressure, temperature and humidity sounding data. However, there are a couple of significant differences between the corrections worth mentioning. In the ground check phase, no ground check correction is applied for the RS41 temperature measurement. A functionality check and a comparison of readings with the temperature sensor of the humidity sensor chip are performed instead. Another major difference is related to the approach on how the humidity measurements take into account the effect of solar radiation. In the case of the RS92, the increment in humidity sensor temperature is estimated taking into account the solar radiation intensity and the related physics, and the humidity measurement result is corrected accordingly. On the contrary, the RS41 humidity sensor incorporates an on-chip temperature sensor, and, thus, the temperature of the humidity sensor is continuously measured and taken into account in the relative humidity calculations. In other words, no solar radiation correction is needed nor applied for the RS41 humidity measurement.

A notable difference in the two sounding systems is that the launch procedure for the RS41 radiosonde is much simpler than that for the RS92. In particular, the RS41 is powered with integrated batteries removing the need to open the body and connect the battery as in the RS92. The RS41 also has status LED indicators which indicate launch readiness as the radiosonde goes through the ground check procedure and self-diagnostics prior to launch. Also, the RS41 ground check device enables an accurate zero humidity check without the use of a desiccant, as in the GC25 ground check device used with the RS92. This change removes the need for maintenance of the desiccant,

a source of operator error. For routine operations the upgrade to RS41 will result in significant savings in time for the operator and less training needed for new operational staff.

3 Experimental design

In order to directly compare observations from the RS41 and RS92 radiosondes, a twin sounding method, which is a simplified version of the World Meteorological Organization Radiosonde Intercomparison test method (Nash et al., 2010), is used. For the experiment, two separate DigaCORA sounding systems were used, an MW31, including an SPS311 sounding processing subsystem, a sounding workstation (laptop) running DigiCORA software v3.66, and a GC25 ground check device, and an MW41 including an SPS311 sounding processing subsystem, a sounding workstation (laptop) running MW41 sounding software v2.1.0 and a RS41 ground check device (Fig. 2). The systems were set up to share one set of UHF Antenna (RM32) and omnidirectional GPS antenna (GA31) as shown in Fig. 2.

The twin sounding method required special equipment and rigging. During the intercomparison study both types of radiosonde (RS41 and RS92) were flown together on a single 600 gram Totex balloon. A heavy duty Graw UW1-30 ozone unwinder was used with 30 m of unwinder string. This was attached to a 1.5 m wooden rod from which the radiosondes were hung at equal distance below the balloon. A parachute was also included to slow the descent of the rigging after the balloon burst. Figure 3 shows a schematic of the equipment used for the twin radiosonde flights. It should be noted that measurement conditions of a radiosonde are not exactly the same in twin sounding as in single radiosonde soundings. In general, due to higher payload and thus more stable flight, sensors have less ventilation in a twin sounding. This may introduce the effects of some error sources (for example temperature sensor orientation error caused by solar radiation). Figure 4 shows a photograph of the launch of a twin-sounding rig from the ARM SGP site.

From 3–7 June 2014, a series of weather balloon flights were performed at the ARM SGP Central Facility (36.695° latitude, −97.485° longitude) with the goal of evaluating the relative performance of the RS92/MW31 and RS41/MW41 radiosondes/systems. The June time period at SGP represented a summertime mid-latitude convective environment during which the extensive remote sensing observations at the SGP site were used to further quantify the environment during the intercomparison. Over the course of five days a total of 20 balloon flights were completed with efforts to sample the entire diurnal cycle and a variety of cloud conditions (avoiding heavy precipitation, which could result in launch failures).

Table 5 summarizes the basic characteristics of the 20 radiosonde flights at the ARM SGP site. Efforts were made to sample the daytime diurnal cycle and also to include several nighttime flights where heating by solar radiation would not be an issue. All 20 flights were considered successful with sampling through the atmosphere to a height of at least 28 km for 19 of the 20 soundings (the final flight terminated at a height just below 26 km). Over the course of five days, a range of different meteorological conditions was observed. Figure 5 shows the time series of (a) precipitable water vapor as retrieved from a two-channel microwave radiometer (Turner et al., 2007), (b) surface dry-bulb temperature and relative humidity, (c) hemispheric sky cover as observed from a total sky imager (Long et al., 2001). Table 6 shows the numerical values of these quantities at the launch time for each sounding. A variety of conditions were sampled including six nighttime soundings, surface temperatures ranging from 20.4 to 33.1 °C, surface relative humidity ranging from 46–96 %, precipitable water vapor ranging from 2.55 to 4.77 cm and hemispheric sky cover ranging from 2 to 100 %. Figure 6 shows hourly profiles of cloud frequency of occurrence derived from the Active Remote Sensing of CLouds value-added data product (Clothiaux et al., 2000; Kollias et al., 2007) that uses a combination of Ka-band Zenith Pointing Radar (KAZR), Micropulse Lidar (MPL) and ceilometer observations to produce a best estimate of cloud occurrence. Occurrence statistics are determined over a 1 h time window and a 30 m height window. Vertical black lines represent the times of dual-radiosonde launches.

Launches occurred for a variety of cloud conditions including single- and multi-layer low and high-level clouds.

4 Results

Figure 7 shows a typical example, from the 3 June 2014 at 17:46 LT balloon flight #3, of the observations collected during a weather balloon flight. This profile shows a temperature inversion with a base near 775 mb and a very dry troposphere above. The convective available potential energy (CAPE) exceeds 2200 J kg^{-1} while the convective inhibition (CIN) is approximately −315 J kg^{-1}. Both CAPE and CIN are calculated by characterizing the surface parcel as the maximum virtual temperature in the lowest 1 km and integrating the buoyancy at all observed sounding levels (Jensen et al., 2015b). The RS41 and RS92 radiosondes showed very similar results for all measurement quantities where the differences between the radiosonde types are much smaller than the variability in a single profile.

For the purposes of calculating quantitative differences between the soundings, we interpolate the RS92 profiles to the same time-step as the RS41 and then, using the RS41 GPS-derived heights, onto a common vertical grid with 10 m vertical resolution. Figure 8 shows a summary of the vertical profiles of differences in barometric pressure, dry-bulb temperature, relative humidity, zonal wind speed and meridional wind speed between the RS92 and RS41 measurements. For each quantity we plot the median, 25th/75th percentile and 10th/90th percentile difference over all 20 soundings for each height on the interpolated grid. The RS41 calculated pressure is greater than that observed by the RS92 at all heights (Fig. 8a) for about half (52 %) of the observations. This results in a maximum (minimum) in the median difference [RS92 – RS41] of 0.20 (−0.56) hPa at a height of 5.63 (0.61) km. These differences are well within the defined accuracy of the radiosonde systems (see Table 4) and are consistent with the results of Motl (2014) who report a maximum difference of 0.3 hPa decreasing to zero at higher levels. For dry bulb temperature (Fig. 8b), the median difference as a func-

tion of height does not exceed 0.13 °C below 28 km. This is consistent with the results of Jauhiainen et al. (2014) who showed mean differences did not exceed 0.2 °C during their sounding intercomparison in the Czech Republic. When considering all of the temperature observations at all heights the mean difference is −0.014 °C. The absolute value of the difference exceeds 0.5 °C (the combined uncertainty in RS92 temperature measurements, see Table 2) for only 0.59 % of the observations. The large negative temperature difference (RS41 temperature greater than RS92 temperature) in the 10th percentile curve at 2.2 km comes from flights number 9 and 10. Sixty-seven percent of the RS41 observations below 28 km indicate a larger relative humidity compared to the RS92 (Fig. 8c), with over 90 % of the observations agreeing to within 2 % RH. The peak in the median differences occurs near 10 km. At 2.2 km there is again noticeable feature where the RS41 measurement is significantly moister (8.2 %) than the RS92 that comes from soundings 9 and 10.

Figures 9 and 10 are used to examine the details of the differences during these two flights. For both soundings, the RS92 shows a cooler temperature (Fig. 9b and d) and larger relative humidity (Fig. 9a and c) compared to the RS41 at heights from approximately 2.1–2.3 km. Figure 10 indicates that there is a liquid cloud layer with a cloud top height near 1.8 km most noticeable after 15:00 UTC but also present during intermittent precipitation prior to that. The large temperature (and relative humidity) differences are occurring shortly after passing through the cloud layer into a dry atmospheric layer that begins at approximately 2.1 km. The additional cooling of the RS92 is likely due to the "wet-bulbing" effect whereby the RS92 sensor became wet as it passed through the cloud layer and then is subject to evaporative cooling after entering the dry layer above cloud. Both the RS92 and RS41 radiosondes use a hydrophobic coating on the temperature sensor in order to reduce the "wet-bulbing" effect without impacting the temperature measurements. However, consistent with the results of Edwards et al. (2014), the RS41 is less prone to "wet-bulbing" effects compared to the RS92 during our intercomparison.

Figure 8d and e show the observed differences for the zonal and meridonal wind profiles. The maximum (absolute value) difference below 28 km in the median zonal (meridional) wind speed is 0.086 (0.119) $m\,s^{-1}$ at a height of 14.81(1.22) km. 99.7 (99.5) % of the zonal (meridional) wind speeds agree within 0.5 $m\,s^{-1}$. This is consistent with the results of Motl (2014) who found differences in the wind velocities to be less than 0.1 $m\,s^{-1}$ for all levels. Edwards et al. (2014), using averages over 1 km deep layers, found differences in the zonal (meridional) wind speed to generally be around +0.01 (−0.01 to −0.03). These small differences are not unexpected as the RS92 and RS41 use the same technique to derive winds from GPS location observations.

The overall differences in pressure, dry bulb temperature, relative humidity and wind speeds observed during this study are consistent with those quantified by Motl (2014), Edwards et al. (2013) and Jauhiainen et al. (2014).

The relative peaks in the temperature and relative humidity differences near a height of 10 km are likely related to a combination of increased radiative heating of sensors due to contributions from cloud albedo, "wet-bulbing" effects and sensor response time in regions of strong gradients as the sondes traverse cloud layers. Figure 11 summarizes the frequency of occurrence of cloud layers during the radiosonde flights. Using the ARSCL data product, the number of soundings for which the cloud occurrence exceeds 25 % for the hour of the sonde launch, for each 30 m layer, is shown. This distribution shows a sharp peak near 2 km and a broader peak around 8–10 km. This peak in cloud occurrence at 8–10 km is coincident with broad maximums in the distributions of pressure, temperature and relative humidity differences between the sonde types (Fig. 8a–c) suggesting that sonde measurements in and around clouds represent the largest differences between the two sonde types.

In order to further quantify the impact of clouds on the observed differences between the RS41 and RS92 radiosondes, we categorize the sounding flights by the observed cloud conditions (cc#) based on ARSCL derived profiles of cloud frequency of occurrence during the hour of the sounding launch. We define eight broad cloud categories for the sounding times, summarized in Table 7. The differences in pressure between

the RS92 and RS41 radiosonde measurements show little dependence on the cloud conditions (not shown). Figure 12 shows the differences in temperature between the RS92 and RS41 radiosonde measurements broken down into these eight categories. The cloud categories that include a contribution from sub-freezing level clouds (cc1, cc2, cc4, cc7) show larger differences in the mid-troposphere compared to most of the other categories (cc6 being a notable exception). The two sets of radiosonde observations occurring during cloud conditions that include only clouds above the freezing level (cc3, cc5) show smaller median differences in the temperature. Sounding observations during cloud category 6 show some of the largest differences. In this case, the main cloud layer straddles the freezing level.

Solar heating of the radiosonde sensors has been known to have an impact on radiosonde measurements (e.g. Milosevich et al., 2009). In order to investigate solar heating impacts on the differences between RS92 and RS41 radiosondes, we have computed the differences separately for daytime and nighttime soundings (as indicated in Table 5). As noted in Sect. 2, the two radiosonde types account for solar radiation impacts in different ways. Figure 13 shows the profiles of the median differences in pressure, dry bulb temperature and humidity for daytime (blue) and nighttime (red) soundings. Note that there were only 6 nighttime soundings during the intercomparison and so the nighttime profile differences are noisier as expected. The pressure profiles show distinct differences between day and night with daytime soundings showing negative values ($P_{RS41} > P_{RS92}$) below 4 km followed by positive values to 13.25 km and near zero above that. Nighttime soundings show larger negative values in the lower atmosphere (below 4 km) but then a secondary negative peak between 5 and 12 km. The temperature difference profiles are nearly identical with slightly larger differences ($T_{RS41} > T_{RS92}$) during the daytime below approximately 10 km. In total, 85 (90) % of the daytime (nighttime) temperature observations agree within 0.2 °C. These results are consistent with the results of Motl (2014) and Jauhiainen et al. (2014) who concluded that the daytime temperature differences were higher compared to nighttime but still generally less than 0.2 °C. The daytime-nighttime differences in median relative

humidity are generally less than 1 % (94 % of heights) with the RH_{RS41} almost always greater than the RH_{RS92} showing slightly smaller differences during the nighttime below approximately 5 km and above approximately 12 km (with RH_{RS92} sometimes exceeding RH_{RS41}). It must be noted that although we show smaller differences between the sounding observations at nighttime compared to daytime, that clouds, notably differences in their occurrences for daytime and nighttime observations could be driving the observed differences. Figure 14 shows profiles of the cloud frequency of occurrence compiled over the hour in which a sounding launch occurred for daytime, nighttime and all launches. Both daytime and nighttime profiles include a low-level peak near 2 km. Daytime cases have a broad double peak in the mid- to upper troposphere (5–11 km), similar to cloud category 4, while the nighttime cases have a second peak above 12 km, similar to cloud category 2. While the cloud influences on the radiosonde observations will certainly contribute to the differences shown in Fig. 13, comparisons of individual profiles of daytime and nighttime soundings under similar cloud conditions (not shown) indicate that the day/night differences are persistent.

In order to investigate other environmental factors that may impact the radiosonde observations, we partition the comparison statistics by independent measurements of the precipitable water vapor (PWV) retrieved from microwave radiometer measurements, sky cover (SC) measured by a total sky imager, and surface RH and surface temperature from in situ surface meteorology sensors. For these comparisons we partition the radiosonde observations based on the median (adjusted for significant digits) of the independent measurements at the 20 launch times: 3.6 cm for PWV, 40 % for sky cover, 65.2 % for surface RH and 26.5 °C for surface temperature. Figure 15 shows this comparison for median profiles of dry bulb temperature differences. The median profiles of dry bulb temperature differences show little sensitivity to the environmental PWV (Fig. 15a). The profiles for the lowest and highest PWVs match very closely. For 99 % of the heights, the median temperature differences for the highest and lowest PWV agree to within 0.02 °C. When partitioning the difference profiles by sky cover observations, it should be noted that the TSI does not report sky cover at night, so

the nighttime radiosonde flights are not included in this plot (Fig. 15b). Below approximately 10 km the difference between the RS41 and RS92 observations is slightly more ($T_{RS41} > T_{RS92}$) for radiosonde flights during lower sky cover (SC < 40 %) conditions compared to higher sky cover (SC > 40 %) conditions. This difference, in the same direction as the differences between daytime and nighttime observations (Fig. 13), is likely the result of differences in solar heating impacts on the radiosonde measurements when clouds are present. This conclusion is further supported by the fact that once above the tropopause the differences between the two curves become much smaller. Figure 15c and d show the comparisons partitioned by the surface RH and surface temperature respectively. Consistent with Fig. 15b, for conditions where less cloudiness would be expected (lower surface RH and correspondingly higher surface temperature) there are larger differences ($T_{RS41} > T_{RS92}$) in the troposphere. Figures 16 and 17 show similar comparisons for pressure and relative humidity differences respectively. The pressure differences show little dependence to the PWV and SC. There is some different behaviors when partitioning by surface thermodynamic variables. Larger differences ($P_{RS92} - P_{RS41}$) are seen when the surface relative humidity (temperature) is larger (lower). The RH differences show less sensitivity to the environmental parameters.

Differences between the radiosonde observations may be magnified in certain temperature and/or humidity ranges. In an effort to evaluate this possibility we evaluate the differences in relative humidity as a function of temperature for five different humidity ranges (Fig. 18). We determine the median RH difference ($RH_{RS92} - RH_{RS41}$) for all measurements that fall within a 20 % RH and 10 °C temperature bin, requiring a minimum of 250 measurements from at least 6 different flights in a given bin. With the exception of a small number of points in the 0–20 % RH range and temperatures of −40 to −42, the RS41 shows a higher mean relative humidity compared to the RS92 for all humidity ranges and all temperatures. At low relative humidity (0–20 %) the difference between the two radiosonde types increases with temperature ($RH_{41} > RH_{92}$) to approximately −25 °C where the difference is −1.1 %. The difference then decreases to

a temperature of −45 °C where RH92 > RH41 by 0.1 %. Finally the difference increases to lower temperatures ($RH_{41} > RH_{92}$). In the other three RH ranges (20–40, 40–60, 60–80 %), there is a consistent trend of the difference increasing with temperature to −40 °C and then decreasing to colder temperatures. This difference has a maximum of nearly 2.5 % RH at −35 °C for RH in the range of 40–60 %. These differences are similar in magnitude to those observed by Edwards et al. (2014).

A benefit of performing this intercomparison at the ARM SGP site is the ability to leverage the other measurements that are available. We have already used these observations to classify the atmospheric state and cloud conditions for partitioning statistics in the radiosonde comparisons. Here we use retrieved estimates of PWV from a microwave radiometer as an independent standard to compare the radiosonde observations.

Figure 19 shows a comparison of PWV for the RS92 (red), RS41 (green) and microwave radiometer (blue) for each radiosonde flight. Error bars on the MWR observations represent the range of observed PWV during the first half hour (since the bulk of the water vapor will be in the lower troposphere) of each balloon flight. Several previous comparisons between PWV calculated from radiosonde, MWR and GPS observations have shown general agreement within 1–2 mm (Emardson et al., 2000; Niell et al., 2001; Li et al., 2003; Garcia-Lorenz et al., 2009). For all but one flight (#15) the PWV calculated from both soundings is greater than the mean PWV over the first half hour of the flight calculated from the MWR retrieval. This is consistent with the results of Jensen et al. (2015b) and likely the impact of clouds, which are not accounted for in the applied corrections. Previous comparison studies done in much drier conditions (Survo et al., 2015) showed slightly lower PWV measurements from the MWR compared to both the RS41 and RS92 radiosondes. For 14(11) of the flights the PWV calculated from the RS41(RS92) is greater than the largest PWV retrieved from the MWR over the first half hour of the flight. The PWV from the RS41 exceeds that from the RS92 for 11 of the flights with the differences ($PWV_{RS92} - PWV_{RS41}$) ranging from −0.74 to +0.49 mm. This agreement is well within the RS92 PWV uncertainty of ±2 mm (Yu

et al., 2014) based on Global Climate Observing System (GCOS) Reference Upper-Air Network (GRUAN) RH uncertainly estimates.

5 Summary and conclusions

The Vaisala RS41 radiosonde was developed to replace the RS92 radiosonde, aimed at improving the accuracy of measurements of profiles of atmospheric temperature, humidity and pressure. In order to help characterize these improvements, an intercomparison campaign was undertaken at the ARM SGP site in North Central Oklahoma USA in June 2014. During this campaign, a total of 20 dual radiosonde flights were performed in a variety of atmospheric conditions representing typical midlatitude continental summertime conditions. The results suggest that the RS92 and RS41 measurements generally agree within manufacturer specified tolerances with notable exceptions when exiting liquid cloud layers where the "wet bulbing" effect is mitigated in the RS41 observations. The RS41 also appears to show a smaller impact from solar heating. These results suggest that the RS41 does provide important improvements, particularly in cloudy conditions, but under most observational conditions, the RS41 and RS92 measurements agree to within the manufacturer specified limits and so a switch to RS41 radiosondes will have little impact on long-term observational records.

The sounding dataset collected during this intercomparison (Jensen and Toto, 2015) is available from the ARM PI data archive (http://www.arm.gov/data/pi). All other ARM datasets (those used in the analysis and others) are available from the ARM archive (www.archive.arm.gov) and can be found using the ARM data discovery tool.

Acknowledgements. Participation by M. Jensen, D. Holdridge, T. Toto and K. Johnson was funded by the DOE ARM Program. S. Baxter was supported by the DOE, Office of Science, and Office of Workforce Development for Teachers and Scientists (WDTS) under the Science Undergaduate Laboratory Internship (SULI) Program. Data were obtained from the ARM program sponsored by the US Department of Energy, Office of Science, Office of Biological and Environmental Research, Climate and Environmental Sciences Division. The DOE ARM Program provided RS92 radiosondes, balloons, unwinders and parachutes. We would also like to acknowledge the technical support from ARM SGP Central Facility operations staff, logistical support from the BNL Office of Educational Programs, and support in campaign arrangements from Vaisala.

References

Ackerman, T. P. and Stokes, G. M.: The atmospheric radiation measurement program, Phys. Today, 56, 38–45, 2003.

Clothiaux, E. E., Ackerman, T. P., Mace, G. G., Moran, K. P., Marchand, R. T., Miller, M. A., and Martner, B. E.: Objective determination of cloud heights and radar reflectivities using a combination of active remote sensors at the ARM CART sites, J. Appl. Meteorol., 39, 645–665, 2000.

Dunn, M., Johnson, K. L., and Jensen, M. P.: The Microbase Value-Added Product: A Baseline Retrieval of Cloud Microphysical Properties, US Department of Energy, Office of Science, Office of Biological and Environmental Research, Gaithersburg, MD, USA, DOE/SC-ARM/TR-095, 2011.

Edwards, Anderson, D. G., Oakley, T., and Gault, P.: Met Office Intercomparison of Vaisala RS92 and RS41 Radiosondes, Met Office, Exeter, UK, Met Office Report, 89 pp., 2013.

Elliott, W. P. and Gaffen, D. J.: On the utility of radiosonde humidity archives for climate studies, B. Am. Meteorol. Soc., 72, 1507–1520, 1991.

Elliot, W. P., Ross, R. J., and Schwartz, B.: Effects on climate records of changes in national weather service humidity processing procedures, J. Climate, 11, 2424–2436, 1998.

Emardson, T. R., Johansson, J., and Elgered, G.: The systematics behavior of water vapor estimates using four years's of GPS observations, IEEE T. Geosci. Remote, 38, 324–329, 2000.

Gaffen, D. J.: Historical changes in radiosonde instruments and practices, World Meteorological Organization, Geneva, Switzerland, WMO Instruments and Observing Methods Rep., 50, 123 pp., 1993.

Garcia-Lorenzo, B., Castro-Almazan, J. A., Eff-Darwich, A., Munoz-Tunon, C., Pinilla-Alonso, N., Rodrigues-Espinosa, J. M., and Romero, I.: Precipitable water vapour content

above the Roque de los Muchachos observatory from GPS estimations, in: Proc. SPIE 7475, Remote Sensing of Clouds and the Atmosphere XIV, 74751H, doi:10.1117/12.830235, 2009.
Ghan, S. J., Randall, D. A., Xu, K.-M., Cederwall, R., Cripe, D., Hack, J., Icobellis, S., Klein, S., Krueger, S. K., Lohmann, U., Pedretti, J., Robock, A., Rotsayn, L., Somerville, R., Stechikov, G., Sud, Y., Walker, G., Xie, S. C., Yio, J., and Zhang, M. H.: An intercomparison of single column model simulations of summertime midlatitude continental convection, J. Geophys. Res., 105, 2091–2124, 2000.
Huang, D., Zhao, C., Dunn, M., Dong, X., Mace, G. G., Jensen, M. P., Xie, S., and Liu, Y.: An intercomparison of radar-based liquid cloud microphysics retrievals and implications for model evaluation studies, Atmos. Meas. Tech., 5, 1409–1424, doi:10.5194/amt-5-1409-2012, 2012.
Jauhiainen, H., Survo, P., Lehtinen, R., and Lentonen, J.: Radiosonde RS41 and RS92 key differences and comparison test results in different locations and climates, TECO-2014, WMO Technical Conference on Meteorological and Environmental Instruments and Methods of Observations, Saint Petersberg, Russian Federation, 7–9 July 2014, P3(16), 2014.
Jensen, M. P.: Comparison of Vaisala RS92 and RS41 Radiosonde at the ARM Southern Great Plains Site, Vaisala News, 194, 4–5, 2015.
Jensen, M. P. and Toto, T.: Soundings from SGP, June 2014 Sounding Intercomparison, 3 June – 8 June 2014, 36°36′18.0″ N, 97°29′6.0″ W: Southern Great Plains Central Facility Atmospheric Radiation Measurement (ARM) Climate Research Facility Data Archive, Oak Ridge, Tennessee, USA, doi:10.5439/1171962, 2015.
Jensen, M. P., Petersen, W. A., Bansemer, A., Bharadwaj, N., Carey, L. D., Cecil, D. J., Collis, S. M., Del Genio, A. D., Dolan, B., Gerlach, J., Giangrande, S. E., Heymsfield, A., Heymsfield, G. M., Kollias, P., Lang, T. J., Nesbitt, S. W., Neumann, A., Poellot, M. R., Rutledge, S. A., Schwaller, M. R., Tokay, A., Williams, C. R., Wolff, D. B., Xie, S., and Zipser, E. J.: The Midlatitude Continental Convective Clouds Experiment (MC3E), B. Am. Meteorol. Soc., accepted, 2015a.
Jensen, M. P., Toto, T., Troyan, D., Ciesielski, P. E., Holdridge, D., Kyrouac, J., Schatz, J., Zhang, Y., and Xie, S.: The Midlatitude Continental Convective Clouds Experiment (MC3E) sounding network: operations, processing and analysis, Atmos. Meas. Tech., 8, 421–434, doi:10.5194/amt-8-421-2015, 2015b.
Kollias, P., Miller, M. A., Luke, E. P., Johnson, K. L., Clothiaux, E. E., Moran, K. P., Widener, K. B., and Albrecht, B. A.: The atmospheric radiation measurement program cloud profiling radars:

second-generation sampling strategies, processing and cloud data products, J. Atmos. Ocean. Tech., 24, 199–1214, doi:10.1175/JTECH2033.1, 2007.
Li, Z., Muller, J.-P., and Cross, P.: Comparison of precipitable water vapor derived from radiosonde, GPS, and moderate-resolution imaging spectroradiometer measurements, J. Geophys. Res., 108, 4651 doi:10.1029/2003JD003372, 2003.
Long, C. N., Slater, D. W., and Tooman, T.: Total Sky Imager Model 880 Status and Testing Results, ARM Technical Report ARM TR-006, US Department of Energy, Washington, D.C, 2001.
Mather, J. H. and Voyles, J. W.: The ARM climate research facility: a review of structure and capabilities, B. Am. Meteorol. Soc., 94, 377–392, 2013.
McCarthy, M. P., Thorne, P. W., and Titchner, H. A.: An analysis of tropospheric humidity trends from radiosondes, J. Climate, 22, 5820–5838, 2009.
McFarlane, S., Sivaraman, C., Chapman, E., Jensen, M. P., Toto, T., Liu, S., and Fischer, M.: Planetary Boundary Layer (PBL) Height Value-Added Product (VAP): Radiosonde Retrievals, US Department of Energy, Office of Science, Office of Biological and Environmental Research, Gaithersburg, MD, USA, DOE/SC-ARM-TR-132, 2013.
Miller, M. A.: SGP Cloud and Land Surface Interaction Campaign (CLASIC): Science and Implementation Plan US Department of Energy. DOE/SC-ARM-0703, US Department of Energy, Office of Science, Office of Biological and Environmental Research, Gaithersburg, MD, USA, 2007.
Milosevich, L. M., Vomel, H., Whiteman, D. N., and Leblanc, T.: Accuracy assessment and correction of Vaisala RS92 radiosonde humidity measurements, J. Geophys. Res., 114, D11303, doi:10.1029/2008JD011565, 2009.
Motl, M.: Vaisala RS41 trial in the Czech Republic, Vaisala News, 192, 14–17, 2014.
Nash, J., Oakley, T., Vomel, H., and Wei, L.: WMO Intercomparison of high quality radiosonde systems, Yangjiang, China 12 July–3 August 2010, World Meteorological Organization, Geneva, Switzerland, WMO Instruments and Observing Methods Report No. 107. 2010.
Niell, A. E., Coster, A. J., Solheim, F. S., Mendes, V. B., Toor, P. C., Langley, R. B., and Upham, C. A.: Comparison of measurements of atmospheric wet delay by radiosonde, water vapor radiometer, GPS, and VLBI, J. Atmos. Ocean. Tech., 18, 830–850, doi:10.1175/1520-0426(2001)018<0830:COMOAW>2.0.CO;2, 2001.
Rowe, P. M., Miloshevich, L. M., Turner, D. D., and Walden, V. P.: Dry bias in Vaisala RS90 radiosonde humidity profiles over Antarctica, J. Atmos. Ocean. Tech., 25, 1529–1541, 2008.

Sawyer, V. and Li, Z.: Detection, variations and intercomparison of the planetary boundary layer depth from radiosonde, lidar, and infrared spectrometer, Atmos. Environ., 79, 518–528, doi:10.1016/j.atmosenv.2013.07.019, 2013.

Stokes, G. M. and Schwartz, S. E.: The Atmospheric Radiation Measurement (ARM) program: programmatic background and design of the cloud and radiation test bed, B. Am. Meteorol. Soc., 75, 1201–1221, 1994.

Survo, P., Leblanc, T., Kivi, R., Jauhiainen, H., and Lehtinen, R.: Comparison of selected in-situ and remote sensing technologies for atmospheric humidity measurement, in: Proceedings of the 19th Conference on Integrated Observing and Assimilation Systems for the Atmosphere, Ocean and Land Surface, Phoenix, AZ, 4–8 January 2015, 13B.2, 2015.

Turner, D. D., Clough, S. A., Liljegren, J. C., Clothiaux, E. E., Cady-Pereira, K., and Gaustad, K. L.: Retrieving liquid water path and precipitable water vapor from Atmospheric Radiation Measurement (ARM) microwave radiometers, IEEE T. Geosci. Remote, 45, 3680–3690, doi:10.1109/TGRS.2007.903703, 2007.

Vaisala: Comparison of Vaisala Radiosondes RS41 and RS92 White Paper. Ref. B211317EN – B © Vaisala, Helsinki, Finland, 2014.

Wang, J., Carlson, D. J., Parsons, D. B., Hock, T. F., Lauritsen, D., Cole, H. L., Beierle, K., and Chamberlain, E.: Performance of operational radiosonde humidity sensors in direct comparison with a chilled mirror dew-point hygrometer and its climate implication, Geophys. Res. Lett., 30, 1860, doi:10.1029/2003GL016985, 2003.

Xie, S., Zhang, M., Branson, M., Cederwall, R. T., Del Genio, A. D., Eitzen, Z. A., Ghan, S. J., Iacobellis, S. F., Johnson, K. L., Khairoutdinov, M., Klein, S. A., Krueger, S. K., Lin, W., Lohmann, U., Miller, M. A., Randall, D. A., Somerville, R. C. J., Sud, Y. C., Walker, G. K., Wolf, A., Wu, X., Xu, K.-M., Yio, J. J., Zhang, G., and Zhang, J.: Simulations of midlatitude frontal clouds by SCMs and CSRMs during the ARM March 2000 Cloud IOP, J. Geophys. Res., 110, D15S03, doi:10.1029/2004JD005119, 2005.

Xie, S., Hume, T., Jakob, C., Klein, S., McCoy, R., and Zhang, M.: Observed large-scale structures and diabatic heating and drying profiles during TWP-ICE, J. Climate, 23, 57–79, doi:10.1175/2009JCLI3071.1, 2010.

Xie, S., Zhang, Y., Giangrande, S. E., Jensen, M. P., McCoy, R., and Zhang, M.: Interactions between cumulus convection and its environment as revealed by the MC3E sounding array, J. Geophys. Res., 119, 11784–11808, doi:10.1002/2014JD022011, 2015.

Xu, K.-M., Cederwall, R. T., and Xie, S.: An intercomparison of cloud-resolving models with the ARM summer 1997 IOP data, Q. J. Roy. Meteor. Soc., 128, 593–624, 2002.

Yu, H., Ciesielski, P., Wang, J., Kuo, H.-C., Vomel, H., and Dirksen, R.: Evaluation of humidity correction methods for Vaisala RS92 tropical sounding data, J. Atmos. Ocean. Tech., 32, 397–411, doi:10.1175/JTECH-D-14-00166.1, 2014.

Zhang, M. H. and Lin, J. L.: Constrained variational analysis of sounding data based on column-integrated budgets of mass, heat, moisture and momentum: approach and application to ARM measurements, J. Atmos. Sci., 54, 1503–1524, 1997.

Zhang, M. H., Lin, J. L., Cederwall, R. T., Yiou, J. J., and Xie, S. C.: Objective analysis of ARM IOP data: method and sensitivity, Mon. Weather Rev., 129, 295–311, 2001.

Zhao, C., Xie, S., Klein, S. A., McCoy, R., Comstock, J., Deng, M., Dunn, M., Hogan, R., Huang, D., Jensen, M. P., Mace, G. G., McFarlane, S., O'Connor, E., Protat, A., Shupe, M., Turner, D. D., and Wang, Z.: Understanding differences in current ARM ground-based cloud retrievals, J. Geophys. Res., 117, D10206, doi:10.1029/2011JD016792, 2012.

Zhao, T., Dai, A., and Wang, J.: Trends in tropospheric humidity from 1970 to 2008 over China from a homogenized radiosonde dataset, J. Climate, 25, 4549–4567, doi:10.1175/JCLI-D-11-00557.1, 2012.

Table 1. Summary of key physical characteristics of the RS41-SG and RS92-SGPD radiosonde models (based on Table 1 from Jauhiainen et al., 2014).

Radiosonde Characteristic	RS41-SG	RS92-SGPD
Weight	109 g	280 g
Dimensions	272 mm × 63 mm × 46 mm	220 mm × 80 mm × 75 mm
Battery type	Lithium, nominal 3 V (integrated)	Alkaline nominal 9 V (separate battery)
Battery capacity	> 240 min	135 min
Transmitter power	Min. 60 mW	60 mW
Telemetry range (with RB31 antenna)	350 km	350 km
Measurement cycle	1 s	1 s

Table 2. Radiosonde temperature sensor manufacturer specifications (based on Table 3 from Jauhiainen et al., 2014).

Radiosonde Characteristics Temperature	RS41-SG	RS92-SGPD
Sensor Type	Platinum Resistor	Capacitive wire
Range	+60 to −90 °C	+60 to −90 °C
Resolution	0.01 °C	0.1 °C
Response Time[a]	0.5 s	< 0.4 s
Combined uncertainty in sounding[b]	0.3 °C < 16 km 0.4 °C > 16 km	0.5 °C < 16 km 0.5 °C > 16 km
Reproducibility in sounding[c]	0.15 °C > 100 hPa 0.3 °C < 100 hPa	0.2 °C > 100 hPa 0.5 °C < 100 hPa

[a] 63.2 % relative humidity, 6 m s^{-1} flow, 1000 hPa.
[b] 2σ (k = 2) confidence level (95.5 %) cumulative measurement uncertainty.
[c] Standard deviation of differences in twin soundings, ascent rate above 3 m s^{-1}.

Table 3. Radiosonde humidity sensor manufacturer specifications (based on Table 4 from Jauhiainen et al., 2014).

Radiosonde Characteristics Humidity	RS41-SG	RS92-SGPD
Sensor Type	Thin-film capacitor, integrated T sensor and heating functionality	Thin-film capacitor, heated twin sensor
Range	0–100 %	0–100 %
Resolution	0.1 %	1.0 %
Response Time Warm[a]	< 0.3 s	< 0.5 s
Response Time Cold[b]	< 10 s	< 20 s
Combined uncertainty in sounding[c]	4 % RH	5 % RH
Reproducibility in sounding[d]	2 % RH	2 % RH

[a] 63.2 % relative humidity, 6 m s^{-1} flow, 1000 hPa, +20 °C.
[b] 63.2 % relative humidity, 6 m s^{-1} flow, 1000 hPa, −40 °C.
[c] 2σ (k = 2) confidence level (95.5 %) cumulative measurement uncertainty.
[d] Standard deviation on differences in two soundings, ascent rate above 3 m s^{-1}.

Table 4. Radiosonde pressure sensor manufacturer specifications (based on Table 5 from Jauhiainen et al., 2014).

Radiosonde Characteristics Pressure	RS41-SG	RS92-SGPD
Sensor Type	GPS derived	Silicon, Capacitive sensor
Range	Surface to 3 hPa	1080 to 3 hPa
Resolution	0.01 hPa	0.1 hPa
Combined uncertainty in sounding[a]	1.0 hPa > 100 hPa	1.0 hPa > 100 hPa
	0.3 hPa < 100 hPa	0.6 hPa < 100 hPa
	0.04 hPa < 10 hPa	0.6 hPa < 10 hPa
Reproducibility in sounding[b]	0.5 hPa > 100 hPa	0.5 hPa > 100 hPa
	0.2 hPa < 100 hPa	0.3 hPa < 100 hPa
	0.04 hPa < 10 hPa	0.3 hPa < 10 hPa

[a] 2σ (k = 2) confidence level (95.5 %) cumulative measurement uncertainty.
[b] Standard deviation on differences in two soundings, ascent rate above 3 m s^{-1}.

Table 5. Radiosonde launch characteristics.

Launch no.	Launch Time (LT = GMT – 5 h)	Maximum height (km)	Mean ascent rate ($m s^{-1}$) to 200 hPa
1	3 Jun 12:55	31.096	4.8
2	3 Jun 15:43	29.881	5.6
3	3 Jun 17:46	28.660	4.7
4	3 Jun 22:07 (Night)	29.378	6.4
5	3 Jun 23:59 (Night)	30.334	6.0
6	4 Jun 12:57	29.487	6.2
7	4 Jun 14:50	29.954	6.0
8	4 Jun 17:13	29.808	6.2
9	5 Jun 09:50	28.088	6.1
10	5 Jun 11:34	28.119	5.9
11	5 Jun 14:57	28.729	5.5
12	5 Jun 21:59 (Night)	29.821	6.7
13	5 Jun 23:39 (Night)	29.800	5.6
14	6 Jun 15:26	28.078	6.3
15	6 Jun 19:16	28.799	6.3
16	7 Jun 09:35	28.725	6.0
17	7 Jun 11:16	28.449	6.0
18	7 Jun 20:09	29.697	5.1
19	7 Jun 22:08 (Night)	29.868	6.0
20	7 Jun 23:55 (Night)	25.957	6.1

Table 6. Surface observations of meteorological state for each launch. Pressure, temperature, relative humidity, wind speed and wind direction observations are from THWAPS (Temperature, Humidity, Wind and Pressure Sensor, www.arm.gov/instruments/thwaps). Sky cover from total sky imager and precipitable water vapor from microwave radiometer.

Flight no.	Pressure (hPa)	Temperature (°C)	RH (%)	Wind speed ($m s^{-1}$)	Wind dir. (deg)	Sky cover (%)	Precipitable water vapor (cm)
1	975.95	31.0	60	9.0	173	54.28	3.57
2	973.83	31.8	51	8.5	166	22.54	3.32
3	971.74	31.1	51	10.5	173	10.64	3.24
4	969.07	26.0	70	4.6	174	–	2.76
5	970.07	25.9	65	7.2	191	–	2.85
6	970.12	32.4	46	4.1	223	23.74	3.84
7	969.75	33.1	46	4.0	205	71.99	3.90
8	969.10	32.9	49	4.0	180	99.55	4.17
9	968.44	22.0	96	4.0	74	99.78	4.44
10	968.31	21.7	86	5.5	76	99.65	4.07
11	970.96	28.6	63	3.8	127	1.67	3.68
12	973.60	26.3	81	2.8	59	–	4.56
13	973.40	23.9	88	9.5	79	–	4.77
14	975.02	28.9	56	1.8	295	35.26	3.74
15	972.55	26.6	76	5.0	95	91.53	3.74
16	975.50	20.9	78	7.4	325	17.69	2.94
17	975.58	24.0	65	5.0	320	16.34	2.97
18	976.12	25.1	64	1.6	10	47.64	3.37
19	976.38	22.6	73	3.8	58	–	3.31
20	977.46	20.4	84	1.3	62	–	3.23

Table 7. Simple cloud classifications for radiosonde flight times. Based on hourly cloud frequency of occurrence at radiosonde launch time from the ARSCL data product.

Category	Sounding flight number(s)	Description
1	10, 14	Three distinct cloud layers, low cloud peak below 4 km, mid cloud peak 5–7 km, high cloud peak above 10 km
2	1, 2, 3, 7, 8, 12	Two cloud layers, low cloud peak below 3 km, high cloud peak above 8 km
3	15, 20	Two cloud layers, mid cloud peak 5–7 km, high cloud peak 10–13 km
4	16, 17	Two cloud layers, low cloud peak below 2 km, mid cloud peak 7–8 km
5	4, 5, 6	Single high cloud peak above 9 km
6	18, 19	Single mid-cloud peak 4–8 km
7	11, 13	Single cloud peak below 4 km
8	9	Significant clouds from surface to 13 km

Figure 1. Picture of two radiosonde types: RS92-SGP (left) and RS41-SG (right).

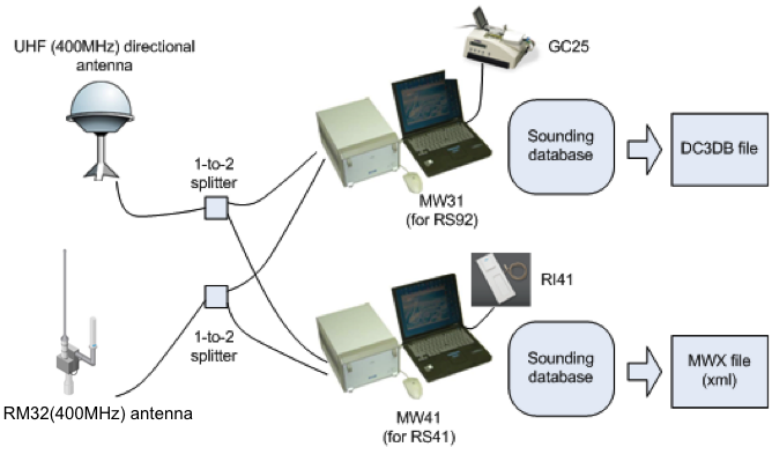

Figure 2. Experimental system set-up: Antennae, Sounding System and Ground Check System.

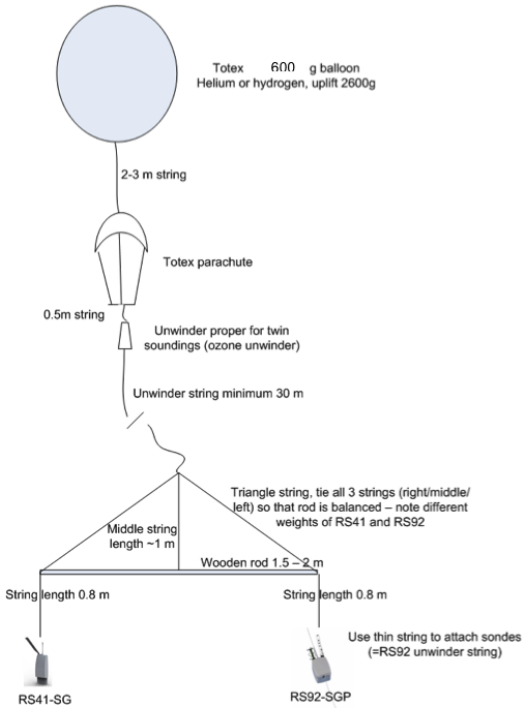

Figure 3. Experimental set-up: Balloon, Parachute, Unwinder, Rigging and Radiosondes.

Figure 4. Radiosonde Launch at the ARM Southern Great Plains site.

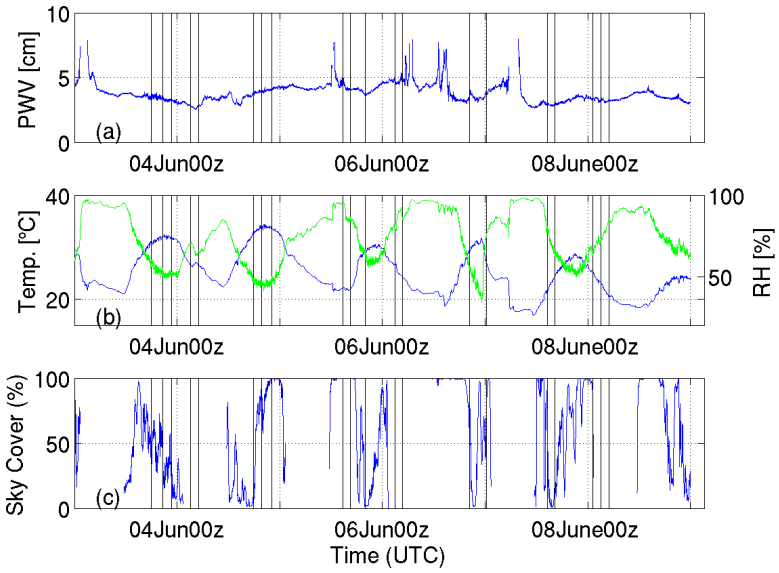

Figure 5. Time series of surface-based meteorological observations **(a)** precipitable water vapor (PWV) retrieved from a 2-channel microwave radiometer, **(b)** surface temperature (blue) and relative humidity (green), **(c)** hemispheric sky cover as observed by a total sky imager (TSI). Vertical black lines represent the times of radiosonde launches.

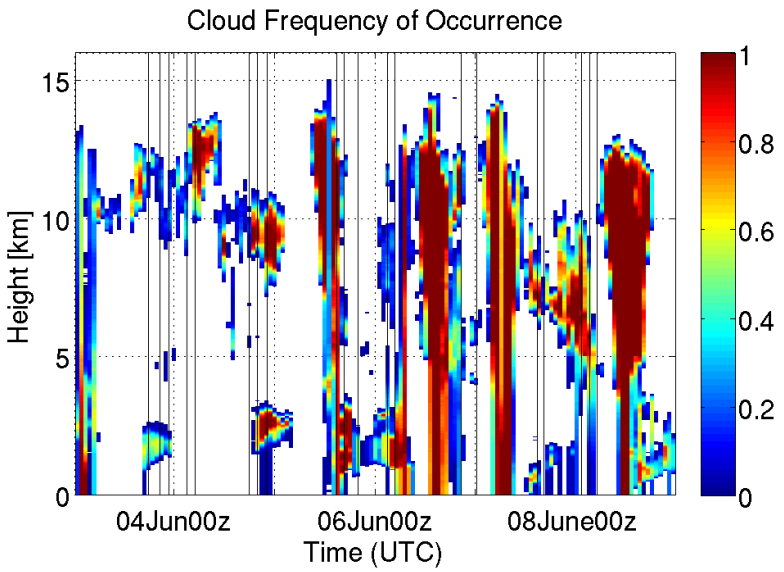

Figure 6. Cloud frequency of occurrence as a function of time and height based on the Active Remote Sensing of CLouds (ARSCL) product which uses a combination of Ka-band Zenith Pointing Radar (KAZR), Micropulse Lidar (MPL) and Ceilometer observations to produce a best estimate of cloud occurrence. Occurrence statistics are determined over a one-hour time window and a 30 m height window. Vertical black lines represent the times of radiosonde launches.

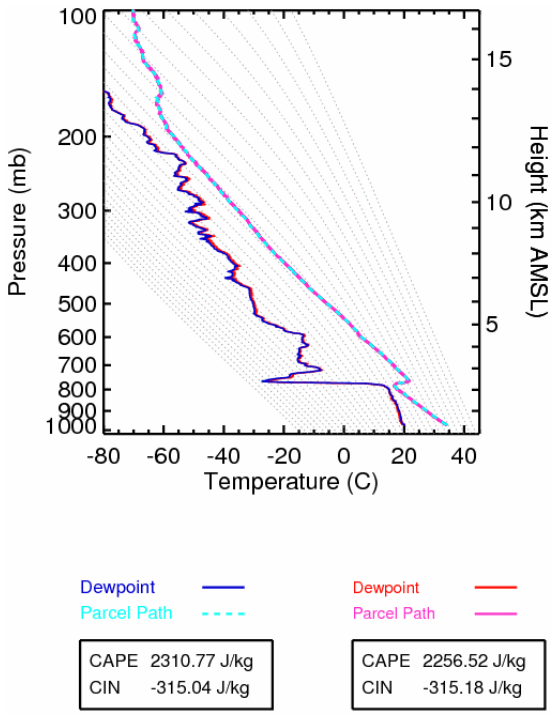

Figure 7. Skew-T plot from balloon flight #3 which was launched on 3 June 2014 at 17:46 LT. Dry bulb temperature for RS92 (cyan) and RS41 (magenta). Dew point temperature for RS92 (blue) and RS41 (red).

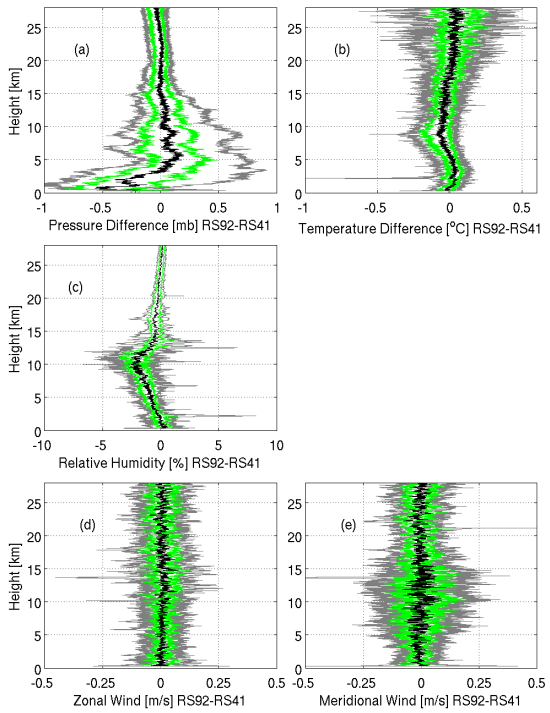

Figure 8. Vertical profiles of the median (black), 25th/75th percentile (green) and 10th/90th percentile (grey) differences between RS92 and RS41 observations (RS92-RS41) for **(a)** pressure, **(b)** dry bulb temperature, **(c)** relative humidity, **(d)** zonal wind and **(e)** meridional wind.

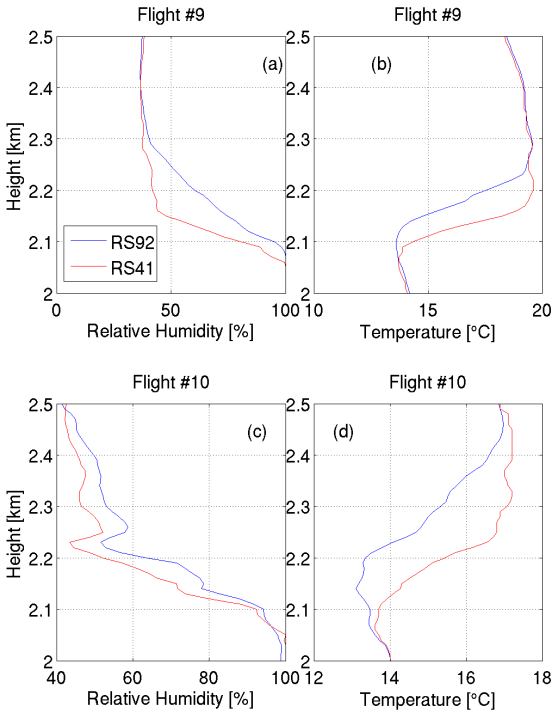

Figure 9. Comparison of relative humidity **(a, c)** and dry bulb temperature **(b, d)** from Flight 9 (top), launch time 14:50 UTC and Flight 10 (bottom), launch time 16:34 UTC.

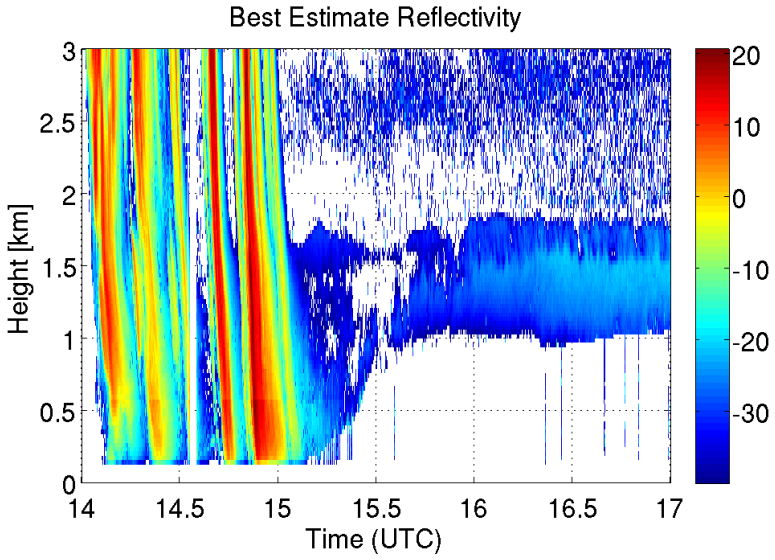

Figure 10. Best estimate radar reflectivity (bottom) from the Ka-band ARM Zenith Pointing Radar Active Remote Sensing of CLouds (ARSCL) product for 5 June 2014.

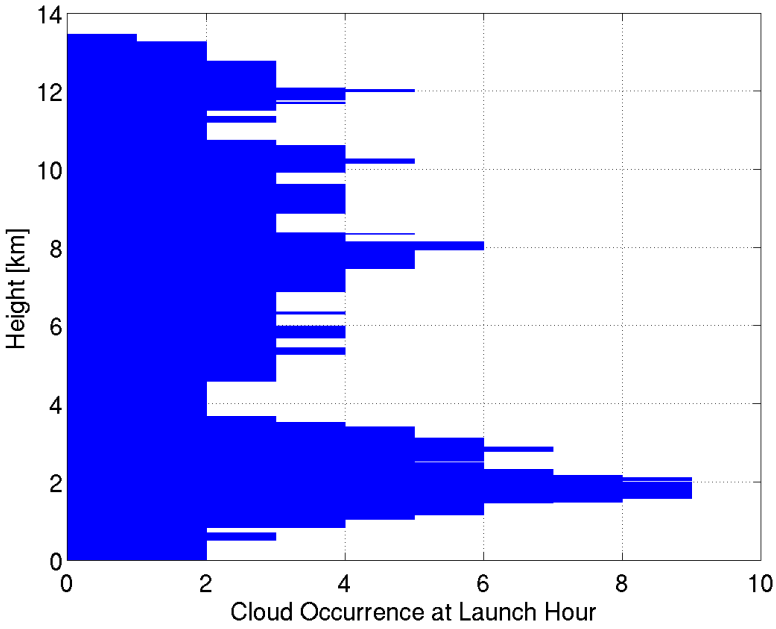

Figure 11. Summary of cloud occurrence at radiosonde launch times. Each bar represents the number of soundings for which the ARSCL product showed cloud occurrence greater than 25 % for the hour of the launch for each height.

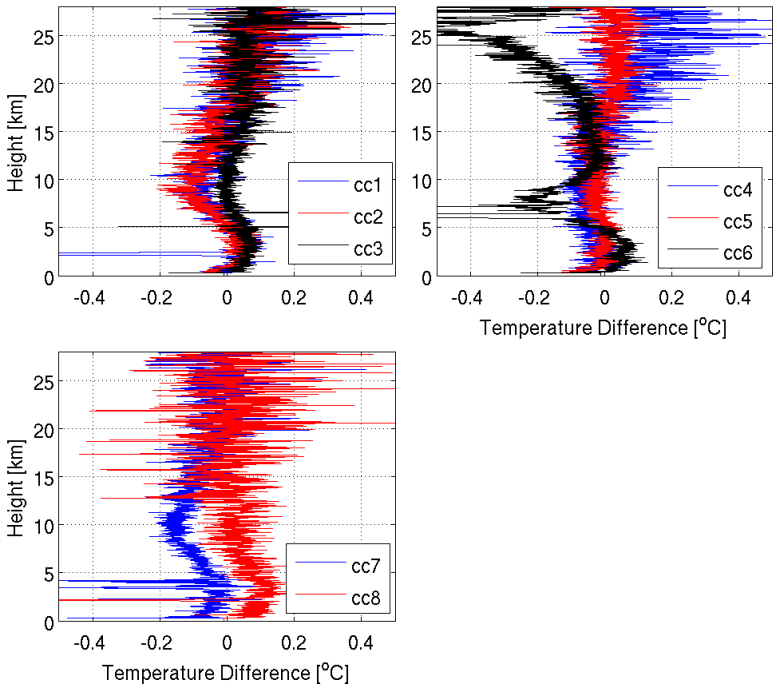

Figure 12. Temperature differences between RS92 and RS41 radiosondes (RS92-RS41) for eight different cloud categories (cc) summarized in Table 7. It should be noted that several of the cloud categories include only a small sample size of one or two soundings.

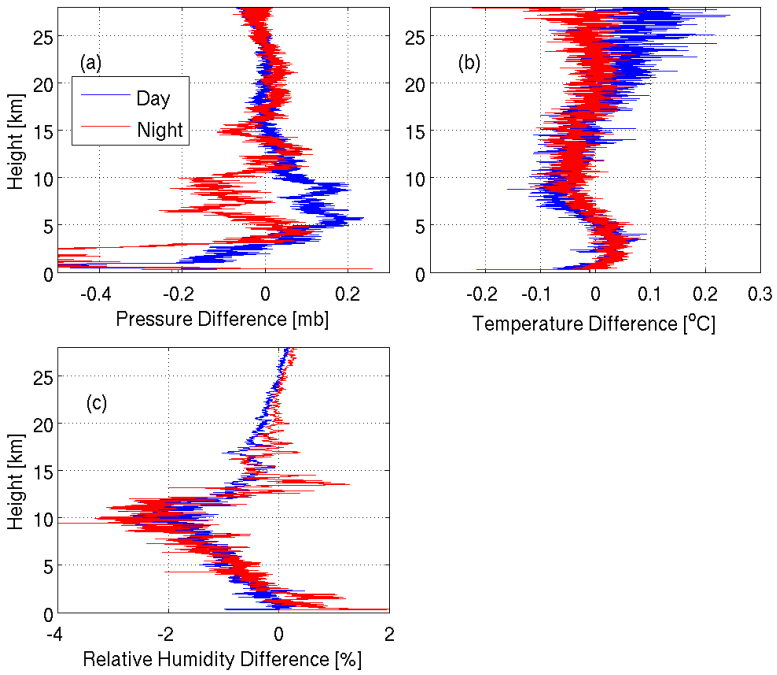

Figure 13. Differences between RS92 and RS41 radiosondes (RS92-RS41) for daytime (blue) and nighttime (red) flights for **(a)** pressure, **(b)** temperature and **(c)** relative humidity.

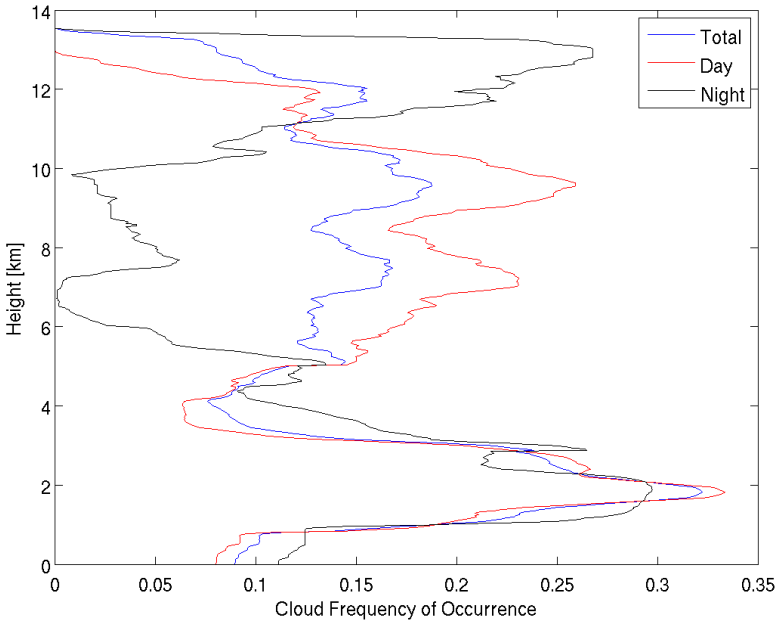

Figure 14. Comparison of cloud frequency of occurrence for daytime, nighttime and all sounding launch times. Cloud frequency of occurrence is calculated using the ARSCL product and compiled over a 1 h window following each sonde launch time.

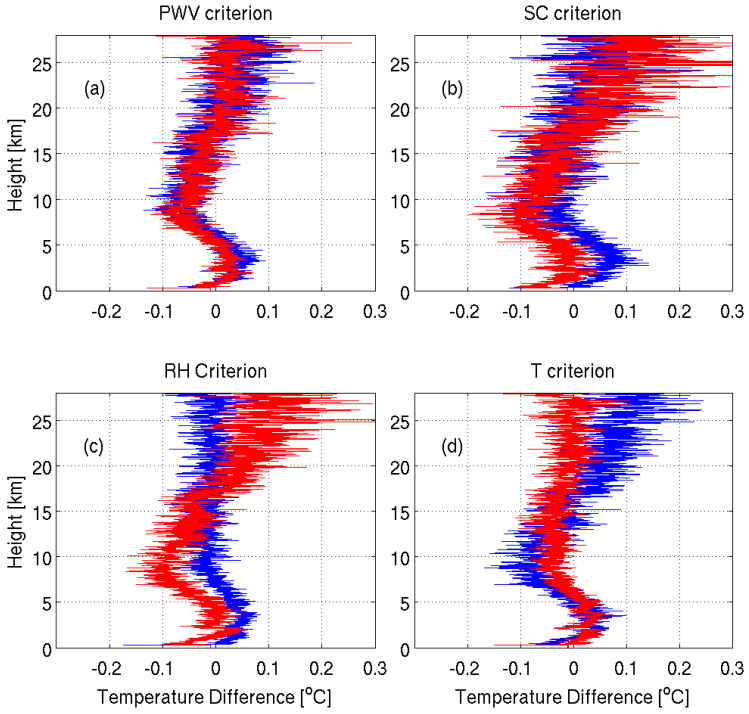

Figure 15. Temperature difference between RS92 and RS41 radiosondes (RS92-RS41) as a function of height for sonde launches with **(a)** PWV > 3.6 cm (blue) and those with PWV < 3.6 cm (red), **(b)** SC > 40 % (blue) and SC < 40 % (red), **(c)** surface RH > 65.2 % (blue) and surface RH < 65.2 % (red), and **(c)** surface temperature > 26.5 °C and surface temperature < 26.5 °C (red). The PWV/SC/RH/T = 3.6 cm/40 %/65.2 %/26.5 °C are based on the median values for the 20 balloon launches during the intercomparison.

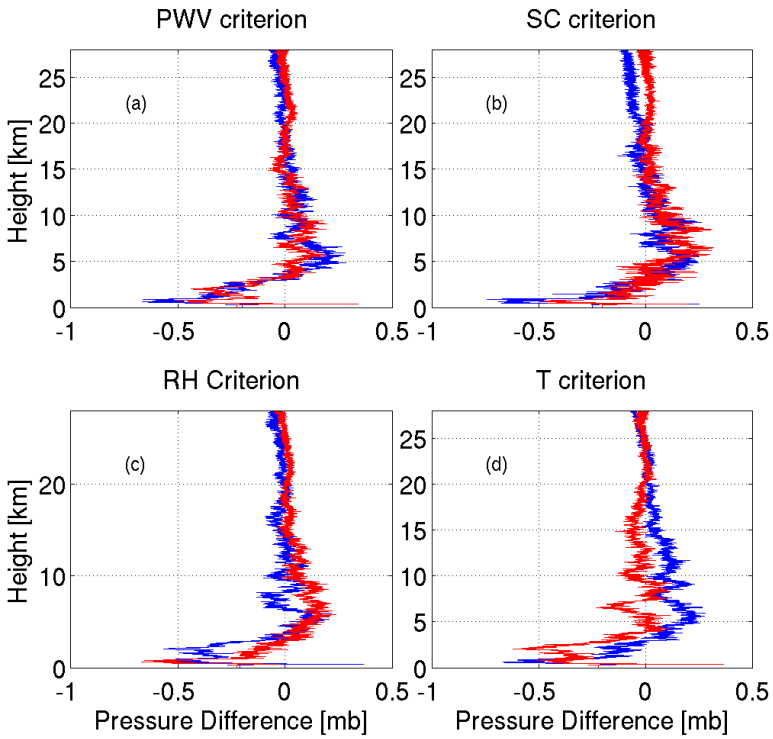

Figure 16. Same as Fig. 15 for pressure differences.

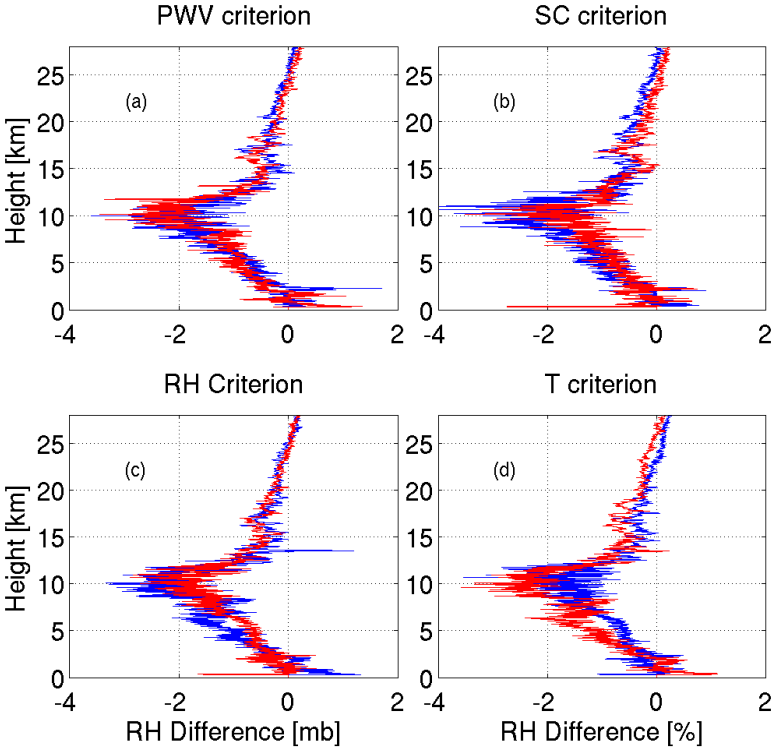

Figure 17. Same as Fig. 15 for relative humidity differences.

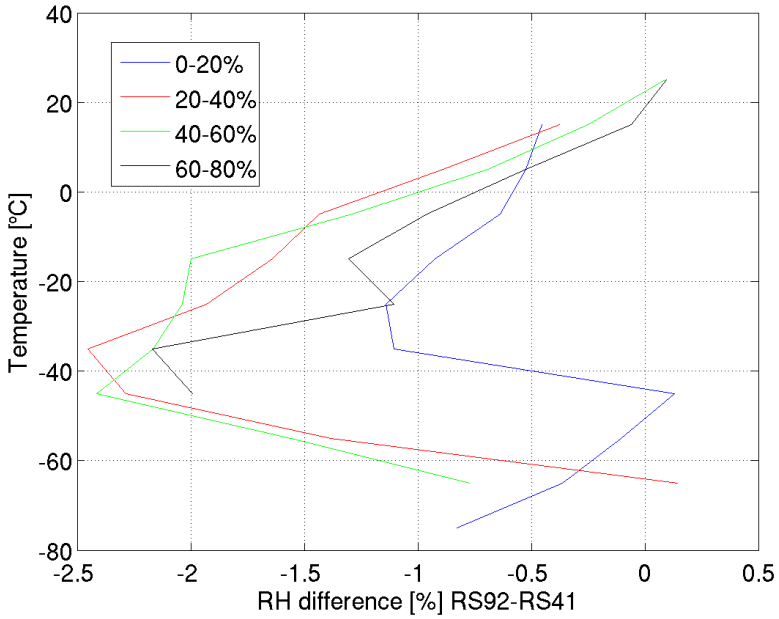

Figure 18. Difference in relative humidity between the RS92 and RS41 radiosondes as a function of temperature for four different relative humidity ranges.

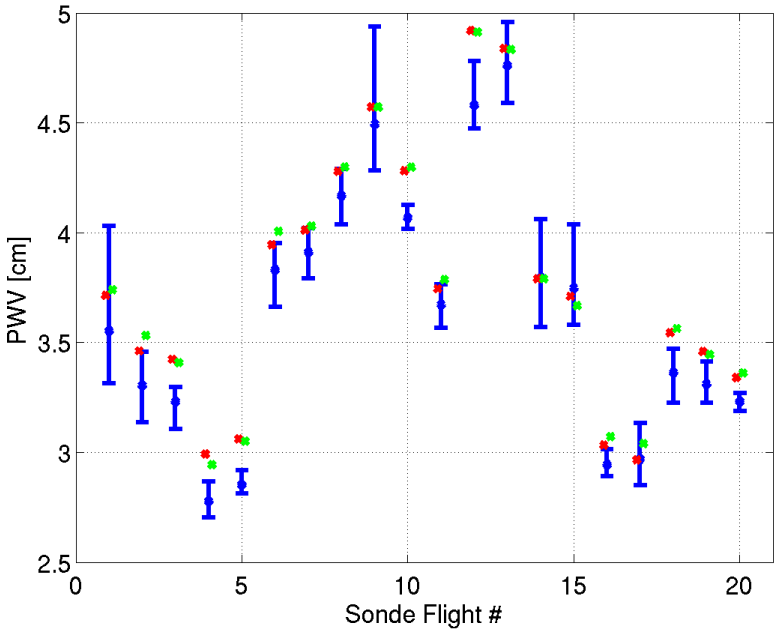

Figure 19. Comparison of precipitable water vapor for the RS92 (red), RS41 (green) and microwave radiometer (blue). Error bars on the MWR observations represent the range of observed PWV during the first half hour of each balloon launch.